Journal of Materials Chemistry A

Materials for energy and sustainability

rsc.li/materials-a

ROYAL SOCIETY OF CHEMISTRY
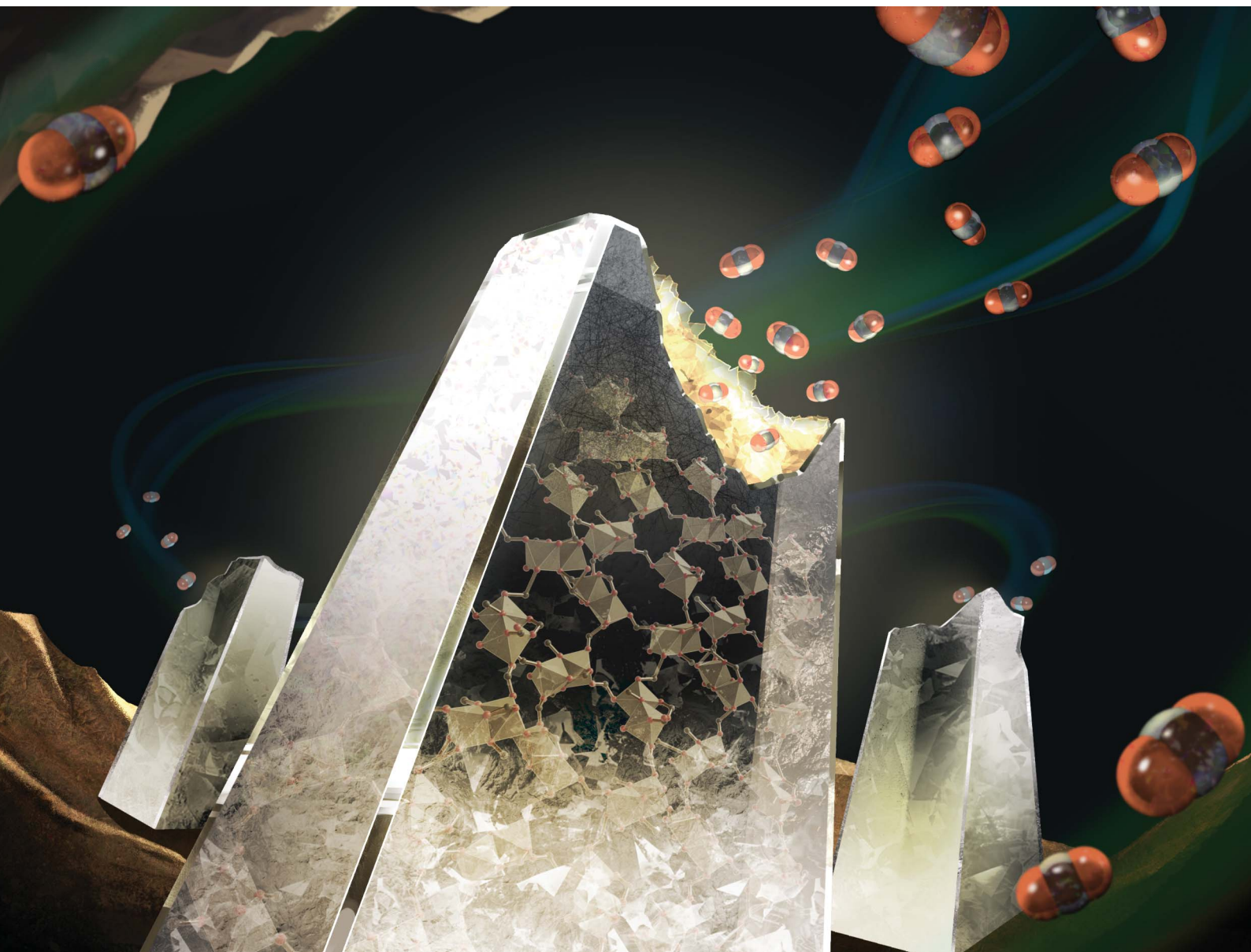
PAPER
Kentaro Kadota, Satoshi Horike *et al.*
Conversion of CO_2 into porous metal–organic framework monoliths

ROYAL SOCIETY
OF CHEMISTRY

PAPER

Conversion of CO$_2$ into porous metal–organic framework monoliths†

Kanchana Sotho, [a] Kentaro Kadota, *[b] Takuya Kurihara, [c] Thanakorn Tiyawarakul, [a] Hiroki Yamada,[d] Kanokwan Kongpatpanich [a] and Satoshi Horike *[abe]

We demonstrate the one-pot conversion of CO$_2$ into amorphous formate-based metal–organic frameworks (MOFs) that form grain-boundary-free monoliths with permanent porosity through hot-pressing. The local coordination geometries of metal ions are characterized using solid-state NMR and synchrotron total X-ray scattering analyses. Hot-pressing decreases the pore sizes of monoliths, enhancing the adsorption selectivity toward H$_2$. The key for the formation of microporous monoliths is the coordination network in which formate, capable of adopting various coordination modes, is connected *via* stable metal–oxygen bonds.

^{a}Department of Materials Science and Engineering, School of Molecular Science and Engineering, Vidyasirimedhi Institute of Science and Technology, Rayong 21210, Thailand

^{b}Department of Chemistry, Graduate School of Science, Kyoto University, Kitashirakawa-Oiwakecho, Sakyo-ku, Kyoto 606-8502, Japan. E-mail: kadota. kentaro.7a@kyoto-u.ac.jp; horike.satoshi.3r@kyoto-u.ac.jp

^{c}Division of Material Chemistry, Graduate School of Natural Science and Technology, Kanazawa University, Kanazawa, Ishikawa 920-1192, Japan

^{d}Diffraction and Scattering Division, Japan Synchrotron Radiation Research Institute (JASRI), Sayo, Hyogo 679-5198, Japan

^{e}Institute for Integrated Cell-Material Sciences, Institute for Advanced Study, Kyoto University, Yoshida-Honmachi, Sakyo-ku, Kyoto 606-8501, Japan

† Electronic supplementary information (ESI) available. See DOI: https://doi.org/10.1039/d4ta08744e

Dr Kentaro Kadota received his PhD in chemistry from Kyoto University in 2020, followed by a postdoctoral fellowship at the University of Oregon from 2020 to 2022. He returned to Kyoto in 2022 as an Assistant Professor at Kyoto University. He has received an Inoue Research Award for Young Scientists. His research interest focuses on the design and synthesis of molecular-based frameworks derived from CO$_2$, as well as their applications for

Kentaro Kadota

CO$_2$ capture and utilization.

1. Introduction

The conversion of CO$_2$ into functional materials is essential for realizing a carbon-neutral society.[1–3] The synthesis of organic polymers and carbon materials from CO$_2$ as a feedstock has been extensively studied in the past few decades.[4,5] In recent years, the synthesis of metal–organic frameworks (MOFs) from CO$_2$ has gained attention.[6] CO$_2$ is converted into bridging linkers, such as formate (OCHO$^-$), formylhydroborate,[7] carbamate,[8] and carboxylate.[9] On the other hand, the inherent inertness of CO$_2$ has restricted the structural diversity of CO$_2$-derived linkers and functionality of the resultant MOFs. An approach to functionalize CO$_2$-derived MOFs that does not rely on the structural diversity of CO$_2$-derived linkers is highly demanded.

Tailoring structural disorder offers a powerful route for functionalizing solid materials. Amorphous materials, such as glasses and gels, lack long-range structural order and exhibit various features, *e.g.*, defects, isotropy, transparency, and high mechanical strength.[10] Amorphous MOFs exhibit unique functionalities that are not achieved by the crystalline analogues. For example, grain-boundary-free monoliths with permanent porosity are formed *via* thermal and mechanical treatment, *e.g.*, melt quenching and hot-pressing.[11,12] The formability and processability of porous monoliths is attractive for enhanced volumetric gas storage capacity and recyclable heterogeneous catalysts.[13,14] Meanwhile, few studies focus on amorphous CO$_2$-derived MOFs and none of them show the formability of porous monoliths.[7,15]

In this work, we attempted to synthesize amorphous CO$_2$-derived MOFs showing permanent porosity as the monolithic form. OCHO$^-$ was selected as a CO$_2$-derived bridging linker. Borohydride (BH$_4^-$) readily converts CO$_2$ into OCHO$^-$ by

This journal is © The Royal Society of Chemistry 2025

J. Mater. Chem. A, 2025, **13**, 13743–13749 | 13743

hydride transfer.[7] The small steric hindrance of OCHO$^-$ allows for various coordination geometries, making it suitable for constructing an isotropic grain-boundary-free structure.[16] Oxophilic Al^{3+} and Ga^{3+} ions were employed to form a strong coordination bond with OCHO$^-$ that is essential to preserve a stable porous structure through hot-pressing treatment.[17]

2. Experimental section

2.1. Synthesis of OCHO$^-$-based MOFs from CO$_2$

All chemicals were obtained from commercial suppliers and used without further purification. The powder samples of OCHO$^-$-based MOFs, denoted as **M-CO$_2$** (M = Al^{3+} and Ga^{3+}), were synthesized from CO$_2$. Sodium borohydride (4.0 mmol) in anhydrous acetonitrile (MeCN, 20 mL) was reacted with CO$_2$ (99.99%) at 2.0 MPa at 25 °C for 1.5 hours in a high-pressure reaction vessel. The resulting suspension was mixed with metal nitrate salts (1.0 mmol) in anhydrous methanol (MeOH, 20 mL) at 100 °C for 48 hours. The white precipitate was isolated by centrifugation, washed with MeOH, and dried under vacuum (45 and 26% yields for **Al-CO$_2$** and **Ga-CO$_2$**).

2.2. General characterization

Thermogravimetric analysis (TGA) was carried out using a Rigaku Thermo plus TG 8122 under N$_2$ flow or air with a heating rate of 10 °C min^{-1}. Differential scanning calorimetry (DSC) was carried out using a Hitachi High-Tech DSC 7200 instrument under N$_2$ flow with a heating/cooling rate of 10 °C min^{-1}. Scanning electron microscopy (SEM) and energy-dispersive X-ray spectroscopy (EDX) was carried out using a JEOL JSM-7610F operated with an acceleration voltage of 200 kV. Transmission Electron Microscopy and Energy-Dispersive X-ray Spectroscopy (TEM-EDS) was carried out using a JEOL JEM-ARM 200F. Fourier transform infrared (FT-IR) spectra were collected using a Bruker ALPHA II FT-IR spectrometer with a Universal ATR accessory under a N$_2$ atmosphere. Inductively coupled plasma-optical emission spectrometry (ICP-OES) was carried out using an Agilent 700 series. The supernatant (200 μL) was dried and digested in a solution of 2% nitric acid with a total volume of 5 mL before a measurement. The average static water contact angle was measured at 25 °C, using a contact angle goniometer by dropping 10 μL of deionized water on three different locations on a monolith. The contact angle of the droplet was analyzed using the Ossila contact angle software.

2.3. X-ray analysis

Powder X-ray diffraction (PXRD) patterns were collected on a Rigaku SmartLab SE X-ray type with CuKα radiation (λ = 1.54059 Å). X-ray photoelectron spectroscopy (XPS) spectra were collected using a JEOL XPS instrument (JPS-9010 MC) with a Mg Kα and Al Kα source (1253.6 eV and 1486.6 eV) under high vacuum (10^{-7} Pa). All binding energy values were referenced to the C 1s peak (284.70 eV). Synchrotron variable-temperature (VT) PXRD patterns were collected using synchrotron radiation (λ = 0.99927 Å) employing a large Debye–Scherrer camera with semiconductor detectors on the BL02B2 beamline at the Super Photon

Ring (SPring-8, Hyogo, Japan). Pair distribution function (PDF) analysis was performed using synchrotron scattering data. Total X-ray scattering was collected at 30 °C with two 2D CdTe detectors at the BL04B2 beamline in SPring-8. The incident energy was 112.9232 keV. $G(r)$ was obtained from the Fourier transform of $S(Q)$ with a Lorch modification function by using IgorPro software. X-ray absorption spectroscopy (XAS) including X-ray absorption near edge structure (XANES) and extended X-ray absorption fine structure (EXAFS) regions was performed in the transmission mode at the BL14B2 beamline at SPring-8.

2.4. NMR analysis

^{1}H, ^{11}B, and ^{13}C solution NMR spectra were collected using a Bruker Avance III HD 600 MHz. The powder samples were digested in 1.0 M DCl/D$_2$O/DMSO-d_6 for NMR measurement. CHN elemental analysis was performed using a LECO TruSpec Micro Element Series with cystine standard. Solid-state ^{1}H, ^{13}C, and ^{27}Al magic-angle spinning (MAS) NMR experiments were conducted on a JEOL JNM-ECZ600R spectrometer at a 14.1 T superconductor magnet at room temperature. ^{13}C cross-polarization (CP)/MAS, ^{1}H–^{13}C 2D CP-heteronuclear correlation (HETCOR), ^{27}Al single-pulse, Harn-echo, and 3QMAS measurements were performed using a JEOL 3.2 mm double resonance MAS probe at a MAS rate of 20 kHz. In the CP/MAS sequence, a ^{1}H 90° pulse width of 2.3 μs and ^{1}H and ^{13}C spin-lock pulse strengths of 70 and 50 kHz with a contact time of 3 ms were used. A ramped-amplitude spin-lock pulse was used for ^{13}C. ^{13}C signals were acquired under ^{1}H TPPM heteronuclear dipolar decoupling pulse irradiation with a pulse strength of 100 kHz. ^{27}Al single-pulse and Hahn-echo MAS spectra were measured with 90° and 180° pulse lengths of 1.15 and 2.3 μs. The ^{27}Al 3QMAS spectrum was obtained using the z-filter 3QMAS sequence. 0 quantum (Q)–3Q excitation, 3Q–0Q reconversion, and weak 90° pulse lengths of 3.3, 1.1, and 8.0 μs were used. ^{27}Al quadrupolar line-shape analysis was performed using ssNake software.[18]

2.5. Catalytic activity of M-CO$_2$ for CO$_2$ cycloaddition

Epichlorohydrin (ECH, 12.5 mmol), **M-CO$_2$** (0.3–1.0 mol%), and tetrabutylammonium bromide (TBAB, 2.0 mol%) were added to the reaction vial (20 mL). CO$_2$ (99.99%) was introduced into the reaction mixture under stirring at 0.1 MPa at 30 °C for 48 hours. The reaction using styrene oxide was carried out at 80 °C. The conversion of ECH into chloropropylene carbonate (CPC) was calculated based on ^{1}H NMR analysis. The recovered catalyst was collected by centrifugation, followed by washing with fresh MeOH and dried in a vacuum.

2.6. Preparation of M-CO$_2$ monolith by hot-pressing

The powder sample of **M-CO$_2$** (20 mg) was introduced into a 7 mm diameter stainless steel die set. A monolith was prepared under air by hot-pressing at 145 °C and 50–55 kN for 2 hours. After pressure release, the die set was taken out to cool down to room temperature.

13744 | J. Mater. Chem. A, 2025, 13, 13743–13749

This journal is © The Royal Society of Chemistry 2025

2.7. Gas adsorption analysis

Gas adsorption isotherms were collected using a MicrotracBEL BELSORP-mini X for N_2 at 77 K and CO_2 at 195, 273, and 298 K. Brunauer–Emmett–Teller surface areas (S_{BET}) were calculated from the N_2 adsorption isotherms. H_2 adsorption isotherms at 77 K were recorded on a MicrotracBEL BELSORP-mini II. The pore size distribution (PSD) was calculated using the non-local density functional theory (NLDFT) method based on the N_2 adsorption isotherms. NH_3 temperature-programmed desorption (TPD) was carried out using a MicrotracBEL BELCAT. NH_3 was captured with 50 mg of powder sample at 40 °C for 30 minutes and the desorption profile was recorded using a TCD detector.

3. Results and discussion

3.1. Synthesis and structural characterization of M-CO₂

The synthesis is a one-pot, two-step procedure involving the insertion of CO_2 into BH_4^- to afford formylhydroborate ($[BH(OCHO)_3]^-$) and subsequent solvothermal reaction that converts $[BH(OCHO)_3]^-$ into $OCHO^-$ (Fig. 1).[7] This method is classified as a type-II (one-pot) synthesis of CO_2-derived MOFs according to the literature.[6] The choice of metal ions and solvents was essential for obtaining amorphous porous structures. A synthetic attempt using Ce^{3+} ion instead of Al^{3+}/Ga^{3+} resulted in a non-porous crystalline product (Fig. S1 and S2†). The larger ionic radius of Ce^{3+} led to a higher coordination number, forming a dense structure. Methoxide (MeO^-), derived from MeOH, serves as a linker in both **M-CO₂** (details below). Control experiments using ethanol (EtOH) instead of MeOH as a synthetic solvent provided amorphous non-porous products

consisting of $OCHO^-$ and Al^{3+} without EtO^- (Fig. S3–S5†). This indicates that the smaller steric hindrance of MeO^- is suitable for constructing the porous structure of **M-CO₂**.

Acid-digested solution NMR was carried out to confirm the formation of $OCHO^-$. The ^1H NMR spectra of **M-CO₂** show peaks at 3.1 and 8.1 ppm corresponding to MeO^- and $OCHO^-$, respectively. The ratios of $OCHO^-$ and MeO^- were calculated as 1 : 1 and 1 : 1.8 for **Al-CO₂** and **Ga-CO₂** (Fig. S6†). The assignment was also confirmed by ^{13}C NMR (Fig. S7†). The ^{11}B NMR spectra showed that **M-CO₂** contained no boron species derived from $NaBH_4$ (Fig. S8†). The FT-IR spectra exhibit the $C=O$ stretching vibration of $OCHO^-$ at 1581 and 1652 cm^{-1} for **Al-CO₂** and **Ga-CO₂**, respectively (Fig. S9†).[19] The broad peak at 3420 cm^{-1} in **Ga-CO₂** was attributed to the O–H stretching vibration of OH^-.[20]

The metal content of **M-CO₂** was determined by pyrolysis under air. TGA heating up to 900 °C under a flow of air fully converted **M-CO₂** into corresponding metal oxides (Fig. S10 and S11†). The gravimetric metal contents were calculated as 19.3 and 59.1 wt% for **Al-CO₂** and **Ga-CO₂**, respectively. Given the results of CHN elemental analysis, the chemical compositions were determined as $[Al_2(OCHO)_3(OMe)_3]$ for **Al-CO₂** and $[Ga_2O_{1.8}(OHCO)_{0.5}(OMe)_{0.9}(OH)]$ for **Ga-CO₂**. The gravimetric CO_2 content was calculated as 46.8 and 9.3 wt% for **Al-CO₂** and **Ga-CO₂** (Table S1†).

The PXRD patterns exhibit broad features at 8.1, 10.8, and 12.3° for **Al-CO₂** and at 5.1° for **Ga-CO₂**, which do not match the reported patterns of metal formate compounds (Fig. 2A and S12†).[19,21,22] SEM-EDX exhibits spherical particles with a diameter of 5 and 2 μm for **Al-CO₂** and **Ga-CO₂** respectively and a homogeneous distribution of each metal element (Fig. 1 and
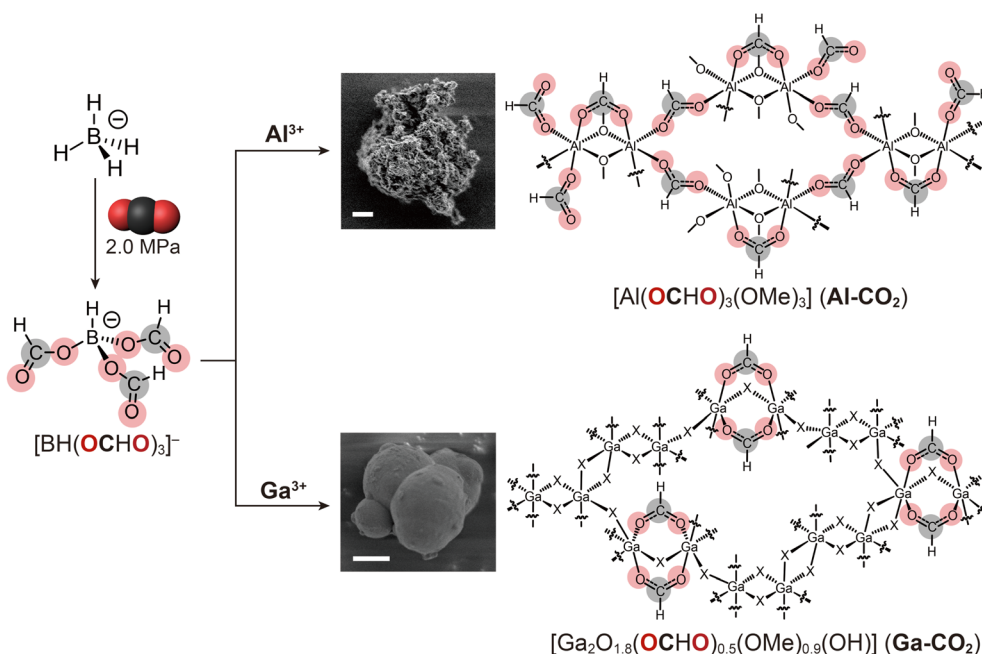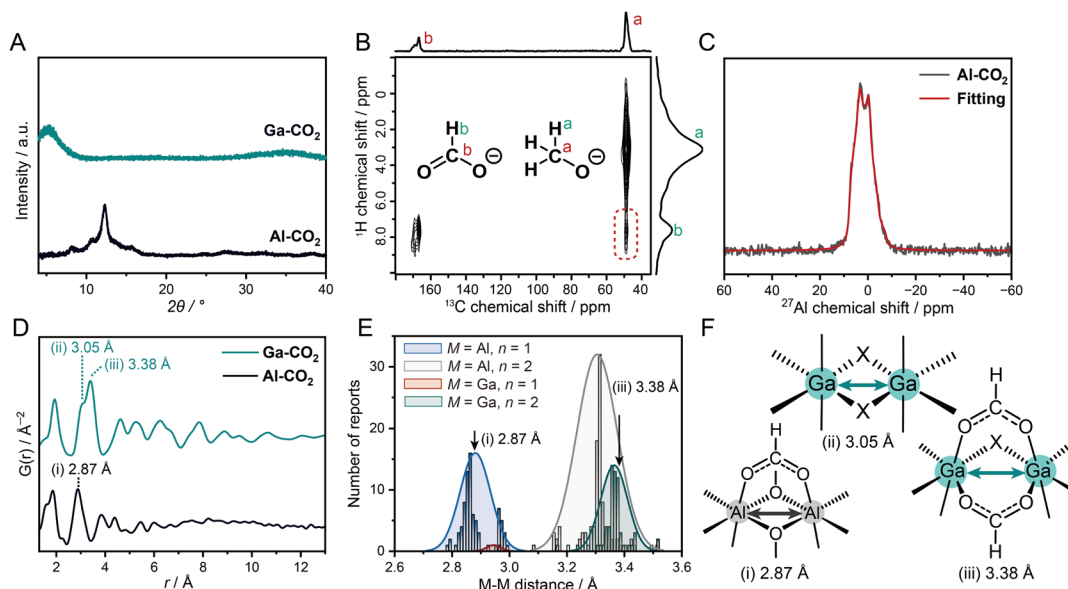

Fig. 1 Schematic illustration of the synthesis and proposed structures of **M-CO₂** (M = Al^{3+}, Ga^{3+}). Carbon and oxygen atoms derived from CO_2 are highlighted. The symbol X in the structure of **Ga-CO₂** indicates either O^{2-}, OH^-, or OMe^-. SEM images of **M-CO₂** are displayed, respectively. The scale bar indicates 1 μm.

This journal is © The Royal Society of Chemistry 2025

J. Mater. Chem. A, 2025, **13**, 13743–13749 | **13745**

Fig. 2 Structural characterization of **M-CO$_2$**. (A) PXRD patterns of **Al-CO$_2$** and **Ga-CO$_2$**. (B) ^{1}H–^{13}C CP-HETCOR NMR spectra of **Al-CO$_2$**. The correlation between ^{1}H of OCHO$^-$ and ^{13}C of MeO$^-$ is highlighted as a green box. (C) ^{27}Al 1D sliced 3QMAS NMR spectrum (black) and fitting (red) of **Al-CO$_2$**. (D) PDF profiles of **Al-CO$_2$** and **Ga-CO$_2$**. (E) Histograms of M–M distances for [M–(R–COO)$_n$(X)$_{3-n}$–M] with Gaussian distribution. (F) Proposed M–M building units of **M-CO$_2$**. X = O^{2-}, OH$^-$, or OMe$^-$.

S13, S14†). TEM-EDS also confirmed the homogeneous distribution of each element in **M-CO$_2$** (Fig. S15 and S16†). Solid-state ^{1}H–^{13}C CP-HETCOR NMR experiment was carried out to examine the intermolecular distance correlation between OCHO$^-$ and MeO$^-$. The ^{1}H–^{13}C HETCOR NMR spectrum of **Al-CO$_2$** exhibits a clear correlation peak between ^{1}H of OCHO$^-$ at 8.5 ppm and ^{13}C of MeO$^-$ at 51.5 ppm (Fig. 2B). **Ga-CO$_2$** also exhibits the correlation between OCHO$^-$ and MeO$^-$ (Fig. S17†). The observed correlations indicate that both OCHO$^-$ and MeO$^-$ are homogeneously distributed to form the structure of **M-CO$_2$**.

The local coordination geometry of Al^{3+} was characterized by ^{27}Al MAS NMR. The ^{27}Al NMR spectrum of **Al-CO$_2$** exhibits an asymmetric line shape due to the ^{27}Al quadrupolar interaction (Fig. S18†). To analyze the coordination structure, we performed quadrupolar line-shape fitting to the ^{27}Al 1D spectrum sliced at the peak center of the isotropic dimension (12.31 ppm) of the 3QMAS spectrum (Fig. 2C and S19†). The isotropic chemical shift $\delta_{iso} = 8.21$ ppm, quadrupolar coupling constant $C_Q = 5.00$ MHz, and asymmetry parameter $\eta = 0.48$ were obtained. The δ_{iso} value suggests that Al^{3+} forms an octahedral six-coordinated geometry.[23,24] The ^{27}Al MAS spectrum of [Al(OCHO)$_3$], possessing the highly symmetric Al^{3+}–6O coordination structure, shows a narrow peak with $C_Q \sim 0$ (Fig. S20†). The larger C_Q value of **Al-CO$_2$** reflects an asymmetric coordination structure of Al^{3+} bound with both OCHO$^-$ and MeO$^-$. The non-zero η suggests a low axial-symmetry structure around Al^{3+} due to the random distribution of the two linkers. The coordination geometry of Ga^{3+} in **Ga-CO$_2$** was characterized by synchrotron XAS. The EXAFS fitting on the first coordination shell confirmed that the coordination number of Ga^{3+} in **Ga-CO$_2$** was 5.6 ± 0.6, which is indicative of octahedral geometry (Fig. S21 and Table S2†). The formation of octahedral geometry in **M-CO$_2$** was also confirmed by XPS (Fig. S22 and S23†). The binding energies of O (1s), C

(1s), and Al (2p$_{3/2}$) were found to be 530.1, 288.0 and 71.6 eV in **Al-CO$_2$** which correspond to Al–O coordination and the presence of OHCO$^-$.[25] **Ga-CO$_2$** shows binding energies of O (1s) and Ga (2p$_{3/2}$) at 531.5 eV and 1118.9 eV which belong to Ga–O bond and Ga^{3+}, respectively.

PDF analysis was performed to characterize the structural periodicity of **M-CO$_2$** (Fig. 2D). The peaks below 2 Å were assigned as the metal–oxygen bonds (1.85 and 1.95 Å for **Al-CO$_2$** and **Ga-CO$_2$**).[26,27] The peaks between 2.0 and 4.0 Å are assigned as metal–metal (M–M) correlations (2.87 Å for **Al-CO$_2$** and 3.05 and 3.38 Å for **Ga-CO$_2$**). To figure out the bridging mode of M–M, we surveyed M–M distances of an Al^{3+}/Ga^{3+}-based coordination compound with octahedral geometry and R–COO$^-$ groups in the CCDC database. The histograms of M–M distances were plotted for the building units of [M–(R–COO)$_n$(X)$_{3-n}$–M] ($M = $ Al^{3+}, Ga^{3+}; X $= $ O^{2-}/OH$^-$/OMe$^-$; $n = 1, 2$, Fig. 2E). We assign the peak at 2.87 Å in **Al-CO$_2$** as [Al–(OCHO)(OMe)$_2$–Al] and 3.38 Å in **Ga-CO$_2$** as [Ga–(OCHO)$_2$(X)–Ga] (Fig. 2E). The peak at 3.05 Å in **Ga-CO$_2$** is assigned as [Ga–(X)$_2$–Ga], edge-sharing octahedral geometry (Fig. 2F and Tables S3, S4†). The mixed coordination of OCHO$^-$ and OMe$^-$ in **Al-CO$_2$** is consistent with the low axial-symmetry structure of Al^{3+} observed by ^{27}Al MAS NMR. The longer-range periodicity was observed up to around 8 and 12 Å for **Al-CO$_2$** and **Ga-CO$_2$**. The extended network is formed by connecting the M–M building units as proposed in Fig. 1.

3.2. Thermal and chemical stability

The TGA profiles under N$_2$ indicate that there was no significant weight loss up to 190 and 180 °C for **Al-CO$_2$** and **Ga-CO$_2$** (Fig. S24†). The thermal stability is slightly lower than those of [M(OCHO)$_3$] (decomposition temperatures: 200 and 230 °C for Al^{3+} and Ga^{3+}).[21] The thermal stability of **Al-CO$_2$** was studied by

13746 | J. Mater. Chem. A, 2025, **13**, 13743–13749

This journal is © The Royal Society of Chemistry 2025

synchrotron variable-temperature PXRD (Fig. S25†). The crystallinity of **Al-CO$_2$** was maintained up to 200 °C and the intensity reduced when heated to 320 °C. The stability of common organic solvents was also studied. The PXRD pattern of **Al-CO$_2$** was intact after soaking in common organic solvents, *e.g.*, tetrahydrofuran, chloroform, and toluene, for 24 h at 25 °C, respectively (Fig. S26†).

3.3. Characterization of the defective open metal site (OMS) for CO$_2$ cycloaddition

We evaluated the Lewis acidity of defective OMS in **M-CO$_2$** by NH$_3$-TPD (Fig. 3). NH$_3$ was completely released below 190 °C within 2 hours, indicating that the defective OMS in **M-CO$_2$** serves as a weak acid site.[28] The total acidic sites were calculated as 0.59 and 2.25 mmol g^{-1} for **Al-CO$_2$** and **Ga-CO$_2$**, respectively. The larger amount of acidic sites in **Ga-CO$_2$** was attributed to a defective OMS in the amorphous structure.[15] Defective OMS serves as a catalytically active site for CO$_2$ cycloaddition with epoxides. The catalytic activity of **M-CO$_2$** was evaluated with ECH as a model reaction. The solvent-free reaction of ECH and CO$_2$ in the presence of 1.0 mol% of **M-CO$_2$** and TBAB as a co-catalyst at 30 °C yielded CPC with a high conversion of 94.4 and 91.6% for **Al-CO$_2$** and **Ga-CO$_2$** (Fig. 3 and S27†). The catalyst amount and reaction time were optimized in the range of 0.3–1.0 mol% and 12–72 h (Fig. S28 and Table S5†). The control experiment using only TBAB without **M-CO$_2$** catalysts resulted in a conversion of 67.5%. The catalytic activity of **M-CO$_2$** maintained the conversion exceeding 90% after three cycles, which is comparable to those of MOFs with catalytically active OMS (Table S7†).[29–31] ICP-OES on the supernatant after the reactions confirms negligible leaching of metal ions from **M-CO$_2$** over three cycles (**Al-CO$_2$**: 0.14–0.33 ppm and **Ga-CO$_2$**: 0.07 ppm, Table S7†).[32,33] **Al-CO$_2$** also exhibited catalytic activity toward the CO$_2$ cycloaddition of styrene oxide into styrene carbonate at 80 °C with conversion of 76.3% (Fig. S29 and Table S6†). Although the diffraction intensity of recycled **Al-CO$_2$** decreased in PXRD, N$_2$ adsorption isotherms and S_{BET} values were comparable after three cycles (Fig. S30 and S31†). In contrast, the recycled **Ga-CO$_2$** exhibited a large decrease in N$_2$ adsorption, whereas the catalytic activity was preserved. This

indicates that the catalytic reaction in **Ga-CO$_2$** mainly occurred at the particle surface rather than internal pores, which is consistent with the catalytic CO$_2$ cycloaddition at the surface of dense MOFs.[34] This is also supported by the smaller pore size of **Ga-CO$_2$** than **Al-CO$_2$** confirmed by N$_2$ adsorption (Fig. S32†). The results indicate that CO$_2$-derived MOFs serve as a catalyst for CO$_2$ cycloaddition under ambient conditions.

3.4. Formability of transparent monoliths

Hot-pressing provided a transparent monolith of **Al-CO$_2$** (Fig. 4A). In contrast, the **Ga-CO$_2$** monolith prepared by hot-pressing under the same conditions was not transparent. The PXRD pattern of the **Al-CO$_2$** monolith exhibits broad features in the same peak positions before hot-pressing, indicative of preservation of the long-range order (Fig. S33†). The differential scanning calorimetry (DSC) profile of **Al-CO$_2$** ground powder does not display any features assignable to the glass transition in the temperature range from −50 to 150 °C (Fig. S34†). The SEM image of the **Al-CO$_2$** monolith displays a grain-boundary-free, smooth surface, resulting in the formation of a transparent monolith (Fig. 4B and S35†). The surface hydrophobicity of the **M-CO$_2$** monolith was tested by a contact angle analysis (Fig. 4C and S36†). The monolithic samples of **Al-CO$_2$** and **Ga-CO$_2$** exhibit water contact angles of 121 ± 0.4 and 116 ± 0.8°, which are categorized as hydrophobic surfaces as the angles are greater than 90°.[35] The hydrophobic feature of **M-CO$_2$** is attributed to the presence of the methyl group of MeO$^-$. The lower hydrophobicity of **Ga-CO$_2$** was due to the OH$^-$ group which can form hydrogen bonding with water molecules.[35]

3.5. Porous properties as powder and monoliths

The porous properties of MOFs as a monolithic form are also essential for wide applications such as catalytic processes and volumetric gas adsorption capacity.[36–38] The gas adsorption measurements were carried out for both powder and monolith samples (N$_2$ at 77 K, CO$_2$ at 195 K, and H$_2$ at 77 K, Fig. 4D, E and S37†). The gas uptake and S_{BET} values calculated from the N$_2$ adsorption isotherms are displayed in Table S8.† The N$_2$ and CO$_2$ uptake of **M-CO$_2$** monoliths largely decreased by 94 and 81% for **Al-CO$_2$** and 85 and 83% for **Ga-CO$_2$**, respectively (Table S8†). This is consistent with the decrease of S_{BET} values of **M-CO$_2$** monoliths, which are reduced by 91% for **Al-CO$_2$** and 80% for **Ga-CO$_2$**. In contrast, **M-CO$_2$** monoliths exhibit a smaller decrease in H$_2$ uptake compared to the reduction in N$_2$ and CO$_2$ uptake (22 and 63% for **Al-CO$_2$** and **Ga-CO$_2$**, respectively). As the kinetic diameters increase (2.89, 3.30, and 3.65 Å for H$_2$, CO$_2$, and N$_2$),[39] larger decreases in gas uptake for both **M-CO$_2$** monoliths were observed. This indicates the pore size reduction of **M-CO$_2$** through hot-pressing, which is consistent with mechanical pressure-induced pore size reduction observed in flexible zeolitic imidazolate frameworks (ZIFs).[40] The key for the preservation of the microporosity of **M-CO$_2$** as the monolithic form is attributed to the coordination network in which OCHO$^-$, capable of adopting various coordination modes, is connected *via* stable Al/Ga–O bonds. Hybrid perovskites composed of OCHO$^-$ exhibit structural transformation in
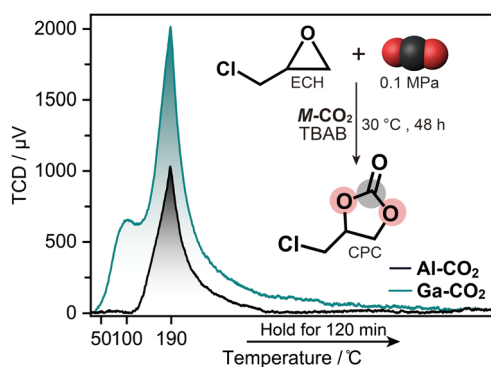

Fig. 3 NH$_3$-TPD profiles of **M-CO$_2$**. Inset: conversion of ECH into CPC *via* CO$_2$ cycloaddition reaction using **M-CO$_2$** catalysis with TBAB as a co-catalyst.

This journal is © The Royal Society of Chemistry 2025

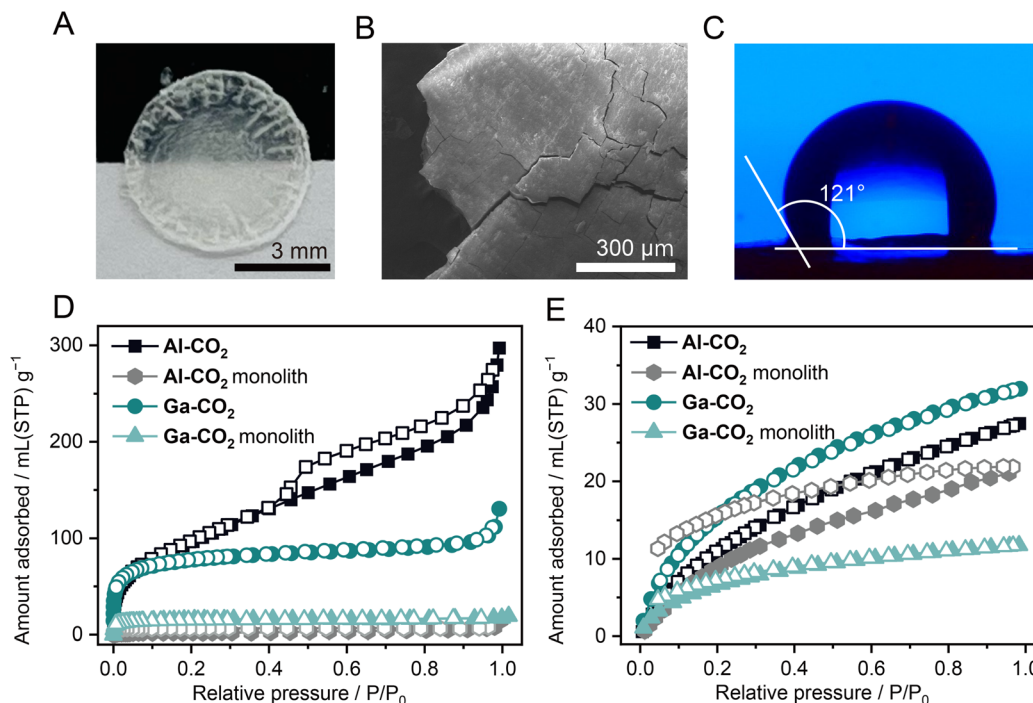*J. Mater. Chem. A*, 2025, **13**, 13743–13749 | **13747**

Fig. 4 (A) Optical image of the transparent **Al-CO₂** monolith with a diameter of 7.0 mm. (B) SEM image of the **Al-CO₂** monolith. (C) Image of a water droplet on the surface of the **Al-CO₂** monolith. (D) N_2 and (E) H_2 adsorption isotherms at 77 K for **M-CO₂** powder and monoliths. Solid/open symbols indicate adsorption/desorption isotherms, respectively.

response to mechanical pressure, driven by alternation in the coordination modes of $OCHO^-$.[41] The flexibility of the coordination geometry of $OCHO^-$ originates from its low steric hindrance.[16] Due to the coordination flexibility and stable Al/Ga–O bonds, hot-pressing does not collapse **M-CO₂** into a nonporous structure, and the microporous structure is maintained while the pore size decreases.

4.   Conclusions

We demonstrated the one-pot synthesis of amorphous MOFs with permanent porosity, $[Al_2(OCHO)_3(OMe)_3]$ (**Al-CO₂**) and $[Ga_2O_{1.8}(OHCO)_{0.5}(OMe)_{0.9}(OH)]$ (**Ga-CO₂**), from CO_2 by converting CO_2 into $OHCO^-$. The local coordination geometries of the metal center were revealed by solid-state NMR and synchrotron total X-ray scattering analysis. **Al-CO₂** formed a grain-boundary-free transparent microporous monolith *via* hot-pressing. Hot-pressing treatment mechanically reduced the pore size of **M-CO₂** monoliths, enhancing adsorption selectivity toward H_2. The key for the formation of the porous monolith was attributed to the coordination flexibility of $OHCO^-$ and stable metal–oxygen bonds. These findings offer a new design guideline for CO_2-derived porous materials by incorporating structural disorder.

Data availability

The data supporting this article have been included as part of the ESI.†

Author contributions

K. K., S. H. and K. S. designed the project. K. S., K. K., T. K., T. T., H. Y., and K. K. contributed to data collection and formal analyses. K. K., S. H. and K. S. wrote the manuscript and all the authors approved the final version.

Conflicts of interest

There are no conflicts to declare.

Acknowledgements

13748 | *J. Mater. Chem. A*, 2025, **13**, 13743–13749

This journal is © The Royal Society of Chemistry 2025

Notes and references

1 J. Artz, T. E. Muller, K. Thenert, J. Kleinekorte, R. Meys, A. Sternberg, A. Bardow and W. Leitner, *Chem. Rev.*, 2018, **118**, 434–504.

2 A. Otto, T. Grube, S. Schiebahn and D. Stolten, *Energy Environ. Sci.*, 2015, **8**, 3283–3297.

3 Q. Liu, L. Wu, R. Jackstell and M. Beller, *Nat. Commun.*, 2015, **6**, 5933.

4 X. Cheng, M. Wu, J. Li, W. Wang, N. Mitsuzaki and Z. Chen, *Catal. Sci. Technol.*, 2023, **13**, 3891–3900.

5 B. Grignard, S. Gennen, C. Jerome, A. W. Kleij and C. Detrembleur, *Chem. Soc. Rev.*, 2019, **48**, 4466–4514.

6 K. Kadota and S. Horike, *Acc. Chem. Res.*, 2024, **57**, 3206–3216.

7 K. Kadota, N. T. Duong, Y. Nishiyama, E. Sivaniah and S. Horike, *Chem. Commun.*, 2019, **55**, 9283–9286.

8 K. Kadota, Y. L. Hong, Y. Nishiyama, E. Sivaniah, D. Packwood and S. Horike, *J. Am. Chem. Soc.*, 2021, **143**, 16750–16757.

9 B. Song, Y. Liang, Y. Zhou, L. Zhang, H. Li, N.-X. Zhu, B. Z. Tang, D. Zhao and B. Liu, *J. Am. Chem. Soc.*, 2024, **146**, 14835–14843.

10 Z. Guo, Z. Liu and R. Tang, *Mater. Chem. Front.*, 2024, **8**, 1703–1730.

11 Y. Zhao, S. Y. Lee, N. Becknell, O. M. Yaghi and C. A. Angell, *J. Am. Chem. Soc.*, 2016, **138**, 10818–10821.

12 Y.-S. Wei, Z. Fan, C. Luo and S. Horike, *Nat. Synth.*, 2023, **3**, 214–223.

13 J. Hou, A. F. Sapnik and T. D. Bennett, *Chem. Sci.*, 2020, **11**, 310–323.

14 D. G. Madden, D. O'Nolan, N. Rampal, R. Babu, C. Camur, A. N. Al Shakhs, S. Y. Zhang, G. A. Rance, J. Perez, N. P. Maria Casati, C. Cuadrado-Collados, D. O'Sullivan, N. P. Rice, T. Gennett, P. Parilla, S. Shulda, K. E. Hurst, V. Stavila, M. D. Allendorf, J. Silvestre-Albero, A. C. Forse, N. R. Champness, K. W. Chapman and D. Fairen-Jimenez, *J. Am. Chem. Soc.*, 2022, **144**, 13729–13739.

15 Z. Fang, Y. Hu, B. Yao, Z. Z. Ye and X. S. Peng, *J. Mater. Chem. A*, 2024, **12**, 6112–6122.

16 A. D. Nicholas, A. Arteaga, L. C. Ducati, E. C. Buck, J. Autschbach and R. G. Surbella III, *Chem.–Eur. J.*, 2023, **29**, e202300077.

17 W. Xu, N. Hanikel, K. A. Lomachenko, C. Atzori, A. Lund, H. Lyu, Z. Zhou, C. A. Angell and O. M. Yaghi, *Angew. Chem., Int. Ed.*, 2023, **62**, e202300003.

18 S. G. J. van Meerten, W. M. J. Franssen and A. P. M. Kentgens, *J. Magn. Reson.*, 2019, **301**, 56–66.

19 V. N. Krasil'nikov, A. P. Tyutyunnik, I. V. Baklanova, A. N. Enyashin, I. F. Berger and V. G. Zubkov, *CrystEngComm*, 2018, **20**, 2741–2748.

20 M. Calatayud, S. E. Collins, M. A. Baltanás and A. L. Bonivardi, *Phys. Chem. Chem. Phys.*, 2009, **11**, 1397–1405.

21 Y.-Q. Tian, Y.-M. Zhao, H.-J. Xu and C.-Y. Chi, *Inorg. Chem.*, 2007, **46**, 1612–1616.

22 K. Kadota, N. T. Duong, Y. Nishiyama, E. Sivaniah and S. Horike, *Chem. Commun.*, 2019, **55**, 9283–9286.

23 S.-Y. Yang, Y. Yan, B. Lothenbach and J. Skibsted, *J. Phys. Chem. C*, 2021, **125**, 27975–27995.

24 M. Haouas, F. Taulelle and C. Martineau, *Prog. Nucl. Magn. Reson. Spectrosc.*, 2016, **94–95**, 11–36.

25 T. Song, Q. Liu, J. Liu, W. Yang, R. Chen, X. Jing, K. Takahashi and J. Wang, *Appl. Surf. Sci.*, 2015, **355**, 495–501.

26 J. A. van Bokhoven, A. M. J. van der Eerden and D. C. Koningsberger, *J. Am. Chem. Soc.*, 2003, **125**, 7435–7442.

27 P. Castro-Fernández, M. V. Blanco, R. Verel, E. Willinger, A. Fedorov, P. M. Abdala and C. R. Müller, *J. Phys. Chem. C*, 2020, **124**, 20578–20588.

28 A. Eskemech, H. Chand, A. Karmakar, V. Krishnan and R. R. Koner, *Inorg. Chem.*, 2024, **63**, 3757–3768.

29 P.-Z. Li, X.-J. Wang, J. Liu, J. S. Lim, R. Zou and Y. Zhao, *J. Am. Chem. Soc.*, 2016, **138**, 2142–2145.

30 X.-Y. Li, L.-N. Ma, Y. Liu, L. Hou, Y.-Y. Wang and Z. Zhu, *ACS Appl. Mater. Interfaces*, 2018, **10**, 10965–10973.

31 G. Zhang, G. Wei, Z. Liu, S. R. J. Oliver and H. Fei, *Chem. Mater.*, 2016, **28**, 6276–6281.

32 S. Kaewsai, S. Del Gobbo and V. D'Elia, *ChemCatChem*, 2024, **16**, e202301713.

33 C. Chen, J. Zhang, G. Li, P. Shen, H. Jin and N. Zhang, *Dalton Trans.*, 2014, **43**, 13965–13971.

34 J. L. Obeso, J. G. Flores, C. V. Flores, V. B. Lopez-Cervantes, V. Martinez-Jimenez, J. A. de Los Reyes, E. Lima, D. Solis-Ibarra, I. A. Ibarra, C. Leyva and R. A. Peralta, *Dalton Trans.*, 2023, **52**, 12490–12495.

35 L.-H. Xie, M.-M. Xu, X.-M. Liu, M.-J. Zhao and J.-R. Li, *Adv. Sci.*, 2020, **7**, 1901758.

36 B. Yeskendir, J.-P. Dacquin, Y. Lorgouilloux, C. Courtois, S. Royer and J. Dhainaut, *Mater. Adv.*, 2021, **2**, 7139–7186.

37 M. I. Nandasiri, S. R. Jambovane, B. P. McGrail, H. T. Schaef and S. K. Nune, *Coord. Chem. Rev.*, 2016, **311**, 38–52.

38 S. Vaidya, O. Veselska, A. Zhadan, M. Diaz-Lopez, Y. Joly, P. Bordet, N. Guillou, C. Dujardin, G. Ledoux, F. Toche, R. Chiriac, A. Fateeva, S. Horike and A. Demessence, *Chem. Sci.*, 2020, **11**, 6815–6823.

39 G. Zheng, J. Wu, Y. Jia, G. Han and S. Zhang, *J. Membr. Sci.*, 2024, **705**, 122924.

40 S. Henke, M. T. Wharmby, G. Kieslich, I. Hante, A. Schneemann, Y. Wu, D. Daisenberger and A. K. Cheetham, *Chem. Sci.*, 2018, **9**, 1654–1660.

41 S. Sobczak and A. Katrusiak, *Inorg. Chem.*, 2019, **58**, 11773–11781.

This journal is © The Royal Society of Chemistry 2025

J. Mater. Chem. A, 2025, **13**, 13743–13749 | **13749**